Ultrafast Carrier Thermalization and Cooling Dynamics in Few-Layer MoS₂

Zhaogang Nie,[†] Run Long,[‡,§] Linfeng Sun,[∥] Chung-Che Huang,[⊥] Jun Zhang,[#,▽] Qihua Xiong,[#,▽] Daniel W. Hewak,[⊥] Zexiang Shen,[∥,#,⊗] Oleg V. Prezhdo,*[,‡] and Zhi-Heng Loh*[,†,#]

[†]Division of Chemistry and Biological Chemistry, School of Physical and Mathematical Sciences, Nanyang Technological University, Singapore 637371, Singapore, [‡]Department of Chemistry, University of Southern California, Los Angeles, California 90089, United States, [§]School of Physics, Complex Adaptive Systems Laboratory, University College Dublin, Belfield, Dublin 4, Ireland, [∥]Centre for Disruptive Photonic Technologies, School of Physical and Mathematical Sciences, Nanyang Technological University, Singapore 637371, Singapore, [⊥]Optoelectronics Research Centre, University of Southampton, Southampton SO17 183, United Kingdom, [#]Division of Physics and Applied Physics, School of Physical and Mathematical Sciences, Nanyang Technological University, Singapore 637371, Singapore, [▽]NOVITAS, Nanoelectronics Centre of Excellence, School of Electrical and Electronic Engineering, Nanyang Technological University, Singapore 639798, Singapore, and [⊗]Division of Materials Technology, School of Materials Science and Engineering, Nanyang Technological University, Singapore 639798, Singapore

ABSTRACT Femtosecond optical pump—probe spectroscopy with 10 fs visible pulses is employed to elucidate the ultrafast carrier dynamics of few-layer MoS₂. A nonthermal carrier distribution is observed immediately following the photoexcitation of the A and B excitonic transitions by the ultrashort, broadband laser pulse. Carrier thermalization occurs within 20 fs and proceeds via both carrier—carrier and carrier—phonon scattering, as evidenced by the observed dependence of the thermalization time on the carrier density and the sample temperature. The $n^{-0.37\pm0.03}$ scaling of the

thermalization time with carrier density suggests that equilibration of the nonthermal carrier distribution occurs via non-Markovian quantum kinetics. Subsequent cooling of the hot Fermi—Dirac carrier distribution occurs on the ~0.6 ps time scale via carrier—phonon scattering. Temperature- and fluence-dependence studies reveal the involvement of hot phonons in the carrier cooling process. Nonadiabatic *ab initio* molecular dynamics simulations, which predict carrier—carrier and carrier—phonon scattering time scales of 40 fs and 0.5 ps, respectively, lend support to the assignment of the observed carrier dynamics.
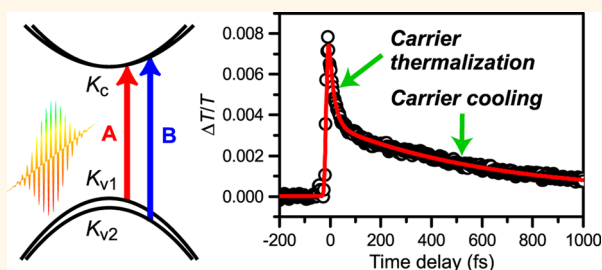
KEYWORDS: MoS₂ · ultrafast dynamics · nonthermal · carrier—carrier scattering · carrier—phonon scattering · quantum kinetics

Inspired by the remarkable electronic properties of graphene,[1,2] explorations of other two-dimensional (2D) materials[3,4] have led to the emergence of few-layer transition metal dichalcogenides as promising candidates for a new generation of optoelectronic materials.[5,6] Of the various few-layer transition metal dichalcogenides, molybdenum disulfide (MoS₂) is the most extensively studied to date.[7] The indirect band gap of bulk MoS₂ (1.3 eV)[8] increases with decreasing number of layers, eventually culminating in the emergence of a 1.8 eV direct band gap semiconductor in the case of single-layer MoS₂.[9,10] The transition from indirect to direct band gap is evidenced by the >10⁴-fold enhancement of the photoluminescence quantum yield for single-layer MoS₂ compared to bulk MoS₂. The existence of a direct band gap in the visible and its relatively strong photoluminescence make single-layer MoS₂ well-suited to a variety of optoelectronic applications.[11,12] Moreover, as a result of the broken inversion symmetry, single-layer MoS₂ possesses two nonequivalent, energetically degenerate valleys at the corners of the first Brillouin zone, labeled K and K′. Coupled with the opposite spin projection of the two spin—orbit—split valence bands, selective photoexcitation of either the K or K′ valley can be achieved with circularly polarized light.[13−16] The ability to address the valley degree of freedom optically suggests a possible route to optoelectronic devices based on valleytronics.[13,17]

The application of few- to single-layer MoS₂ in optoelectronics necessitates a detailed understanding of its fundamental carrier dynamics. For example, ultrafast carrier dynamics are known to determine the electronic transport and optical properties of semiconductors.[18] For applications in
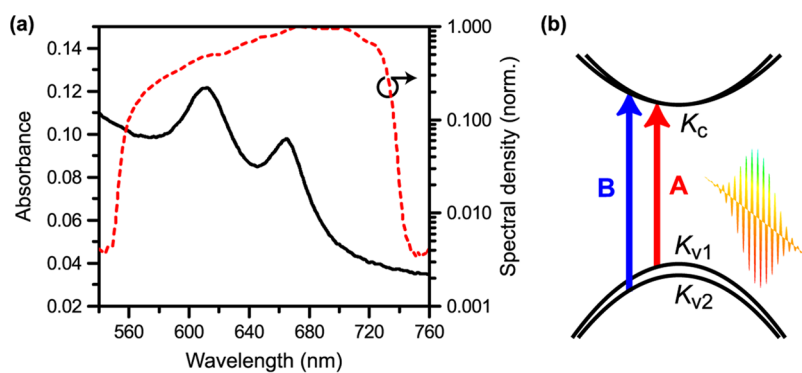
©2014 American Chemical Society

Figure 1. (a) UV/visible absorption spectrum of five-layer MoS_2 sample at 77 K (solid line). The A and B excitonic transitions are located at 665 and 612 nm, respectively. The normalized spectral density of the 10 fs laser pulses employed for pump and probe is also shown (dashed line). (b) The A and B excitonic transitions in MoS_2 correspond to the transitions from the spin−orbit−split K_{v1} and K_{v2} valence bands, respectively, to the conduction band K_c at the K and K′ points.

valleytronics, it is also important to understand how carrier−carrier and carrier−phonon scattering events impact the valley polarization. Motivated by the above considerations, the ultrafast dynamics of single- and few-layer MoS_2 has recently been investigated by several groups. Time-resolved photoluminescence measurements show carrier recombination on a few-picosecond time scale and insignificant polarization decay over the entire emission duration.[19,20] Pump−probe microscopy allows carrier diffusion to be resolved in real space,[21] in addition to the observation of carrier recombination and the trapping of excitons by surface defects.[22] Helicity-resolved optical pump−probe spectroscopy reveals subpicosecond loss of conduction band valley polarization and a slower, ∼10 ps time scale for valence band valley depolarization.[23,24] The observed loss of valley polarization is attributed to trapping of excitons by defect states and Coulomb-induced coupling to dark excitonic states. Finally, a 500 fs decay component observed directly *via* transient absorption spectroscopy has been assigned to exciton−exciton scattering.[25] The above studies on single- to few-layer MoS_2 are complemented by investigations of the ultrafast dynamics of bulk MoS_2. Two-photon photoemission of bulk MoS_2 reveals <100 fs hot-carrier relaxation dynamics,[26] whereas intervalley scattering, carrier cooling, and carrier recombination are observed by transient reflectivity microscopy to occur with time constants of 0.35, 50, and 180 ps, respectively.[27]

Here, we report the application of optical pump−probe spectroscopy with 10 fs, linearly polarized pulses to investigate the earliest ultrafast carrier dynamics that follow the photoexcitation of few-layer MoS_2. The five-layer MoS_2 sample was prepared by chemical vapor deposition and shown by Raman and atomic force microscopies to be highly homogeneous (Supporting Information Figure S1). The large spectral bandwidth of the pump pulse (560−740 nm at −10 dB) allows simultaneous excitation of the A and B excitonic transitions of MoS_2 (Figure 1a and Supporting Information Figure S2), which, for the case of linearly polarized

photoexcitation, correspond to transitions from the two lowest spin−orbit−split valence bands to the conduction band at the K and K′ points (Figure 1b). Typical excitation fluences employed in our experiment yield 2D carrier densities in the range of 10^{13}−10^{14} cm^{-2} (see Supporting Information) which are comparable to or above the 2D Mott density of monolayer MoS_2 (∼10^{13} cm^{-2}).[28] As such, the ultrafast dynamics that are reported here originate from free carriers rather than excitons. Together with excitation fluence- and temperature-dependence measurements, the exquisite time resolution offered by our experiment allows the direct elucidation of carrier thermalization and subsequent carrier cooling dynamics, which are found to occur on <20 fs and ∼0.6 ps time scales, respectively. The assignment of the measured time constants to these processes is further supported by results obtained from *ab initio* non-adiabatic molecular dynamics simulations implemented with time-dependent density functional theory.

RESULTS AND DISCUSSION

The temporal evolution of the differential transmission ($\Delta T/T$) spectrum obtained following photoexcitation of five-layer MoS_2 by 10 fs visible pulses is shown in Figure 2. The positive $\Delta T/T$ reflects ground state bleaching of the A and B excitonic transitions and stimulated emission from the excited states. In addition, a negative $\Delta T/T$ feature, corresponding to excited state absorption, is observed to the low-energy side of the A exciton transition, as well as in between the two excitonic transitions. Recently reported optical pump−probe data obtained after selective excitation of the B exciton transition shows qualitatively similar features.[25] The excited state absorption has been attributed to carrier-induced broadening of the excitonic transitions,[25] or alternatively, to exciton-biexciton transitions.[24] The ultrafast dynamics appear to be biphasic on the time scale of our measurements, which spans <10 fs to 5 ps (see below). In the remainder of this section, the time constants for the fast and slow
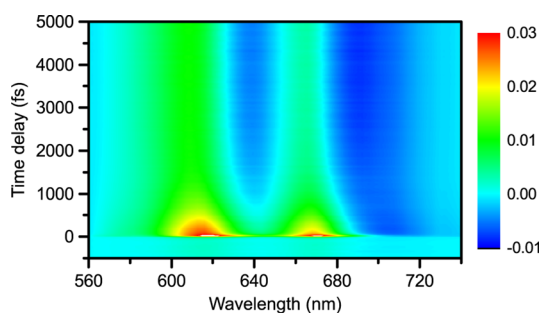
Figure 2. Differential transmission spectra collected as a function of time delay following photoexcitation of five-layer MoS$_2$. The sample temperature is 77 K, and the excitation pump fluence is 0.33 mJ/cm^2.

processes are denoted τ_f and τ_s, respectively. It is important to note here that the free-carrier origin of the ultrafast dynamics entails time constants that are slightly dependent on the probe frequency ω_{pr}. This is because a given ω_{pr} interrogates the carrier dynamics in a specific region of k space where the resonance condition $\hbar\omega_{pr} = E_f(k) - E_i(k)$ is fulfilled; $E_f(k)$ and $E_i(k)$ are the k-dependent energies of the final and initial states that are coupled by the probe transition, respectively. Within the context of carrier thermalization and cooling, the time-dependent differential transmission signal at a given probe wavelength gives the time-evolution of a specific region of the carrier distribution functions.

At short pump–probe time delays ($\tau < 50$ fs), the differential transmission spectra have predominantly positive $\Delta T/T$ values (Figure 3a) and resemble the calculated absorbed laser spectrum (Supporting Information Figure S3). The appearance of these spectra is indicative of saturable absorption and provides strong evidence for the existence of nonthermal carrier distributions.[29,30] Unlike traditional spectral hole-burning that is effected by narrowband lasers,[31] the broadband excitation employed in this work yields a broad spectral hole that overlaps with the ground state bleaching. Moreover, the multitude of ultrafast phenomena—carrier–carrier and carrier–phonon scattering, band gap renormalization, and band filling, all of which are simultaneously operative following the pump excitation, results in complex differential transmission spectra at short time delays. The decomposition of the spectral features in terms of the various ultrafast processes requires further experimental and theoretical investigations that are beyond the scope of this study. Here, we focus on the feature at 655 nm in order to extract time constants that are representative of the ultrafast dynamics at short time delays. A pronounced hole-burning response is expected at this probe wavelength due to its close proximity to the 660 nm center wavelength of the pump pulse.[32] This feature becomes stronger with increasing excitation pump fluence. Its temporal evolution comprises an ultrafast <20 fs decay component τ_f and a slower ~0.6 ps

component τ_s (Figure 3b). The former is hitherto unobserved due to the limited $\gtrsim 100$ fs time resolution employed in previous time-resolved studies, although a recent Z-scan measurement of liquid-phase-exfoliated MoS$_2$ nanosheets suggests carrier relaxation times of ~30 fs.[33] The time constant for the fast decay τ_f decreases with increasing excitation pump fluence F according to the power law $\tau_f \propto F^{-0.37\pm0.03}$ (Figure 3c). The power law can be rewritten as $\tau_f \propto n^{-0.37\pm0.03}$ because the differential transmission signal, and hence the carrier density n, varies linearly with F over the entire range of excitation fluences employed in the experiments (Supporting Information Figure S4). Moreover, temperature-dependence measurements show that τ_f initially decreases with T according to the relation $\tau_f \propto T^{-0.08\pm0.03}$ up to a sample temperature of $T \sim 300$ K, beyond which it exhibits a rapid decrease following $T^{-1.49\pm0.23}$ (Figure 3d).

The appearance of the <20 fs decay component τ_f is assigned to the evolution of the initial nonthermal distribution of carrier energies toward a hot quasi-equilibrium Fermi–Dirac distribution. The measured carrier thermalization time is comparable to those of graphene[34] and graphite,[35] which were found to be <50 and 13 ± 3 fs, respectively. At sufficiently high carrier densities, carrier thermalization is mediated primarily by carrier–carrier scattering, for which ab initio nonadiabatic molecular dynamics simulations predict a characteristic time scale of 37 fs (Figure 3e). As a result of its contribution from carrier–carrier scattering, the thermalization rate is expected to increase with carrier density, as observed in our experimental data (Figure 3c).

The quantitative scaling of carrier–carrier scattering time constants with carrier density for samples of different dimensionalities has been a subject of considerable debate. Femtosecond photon echo measurements performed on bulk GaAs[36] and two-dimensional Al$_x$Ga$_{1-x}$As quantum wells[37] suggests that carrier–carrier scattering times should scale as $n^{-1/D}$, where D is the dimensionality of the sample. This result is consistent with a model that assumes a short-ranged and strongly screened Coulomb interaction that allows carrier–carrier scattering only between nearest neighbors. Within this framework, the carrier–carrier scattering rate scales as $n^{1/D}$ for a D-dimensional sample. The stronger carrier-density dependence observed for a 2D material is rationalized in terms of carrier confinement leading to less effective screening of the carrier–carrier Coulombic interaction. The localization of carriers in MoS$_2$ to a 2D plane, with negligible extension of the carrier wave functions along the interlayer direction in the case of multilayer samples,[38] is therefore expected to yield an $n^{-1/2}$-dependence for the carrier–carrier scattering time constant, in contrast to the $n^{-1/3}$-scaling that is suggested by our experimental results. This expectation, however, is inconsistent with the identical carrier
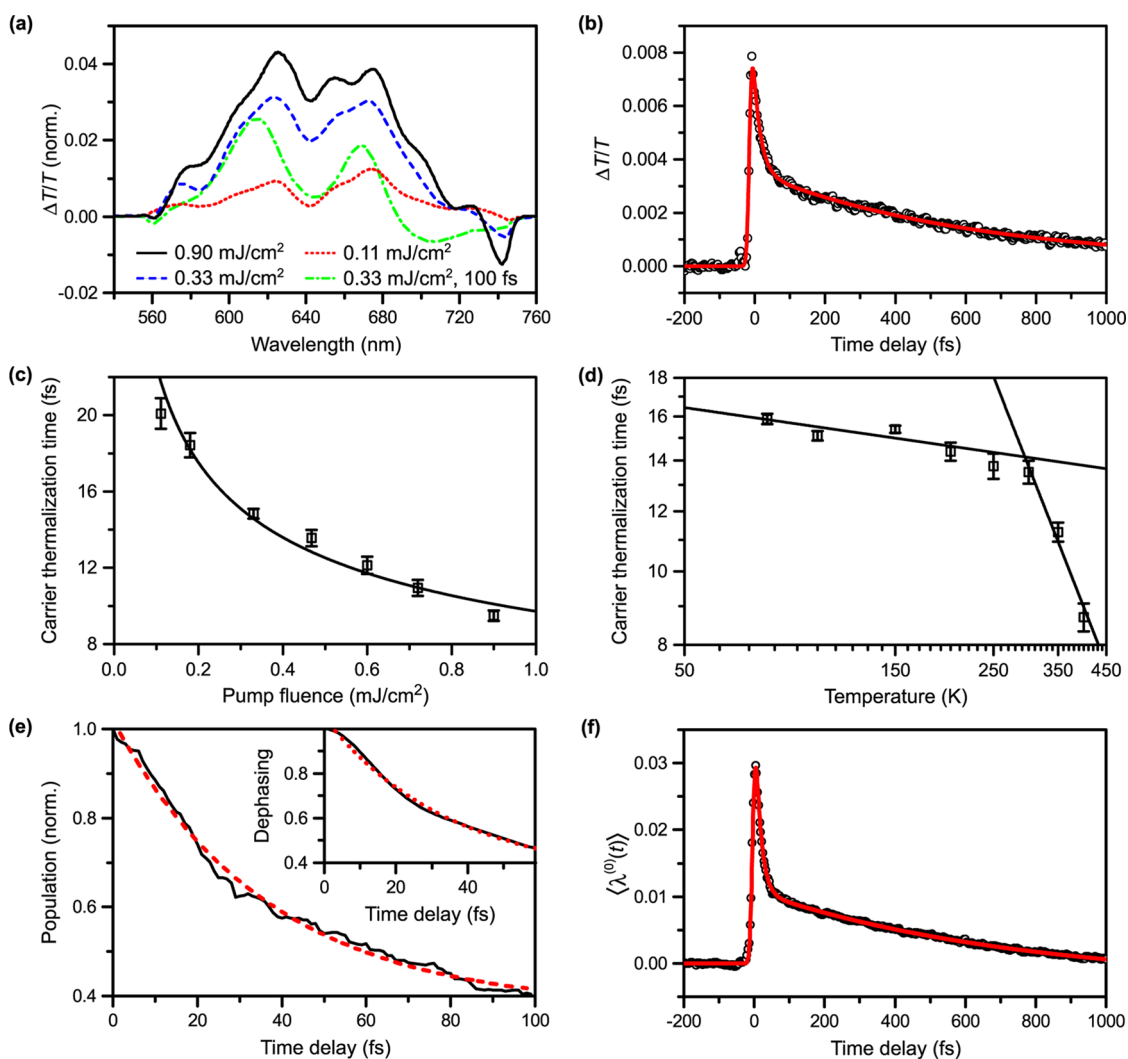
Figure 3. (a) $\Delta T/T$ spectra acquired at 15 fs time delay for various excitation pump fluences at 77 K. The $\Delta T/T$ spectrum acquired at a time delay of 100 fs, representative of a thermalized carrier distribution, is also shown for comparison. (b) $\Delta T/T$ time trace obtained at 655 nm probe wavelength with 0.11 mJ/cm^2 excitation fluence and 77 K sample temperature. The solid line is a fit to a biexponential decay convolved with the instrument response function. (c) Dependence of the fast decay component τ_f on excitation fluence F at 77 K. The solid line is a fit to the power law $\tau_f \propto F^{-0.37\pm0.03}$. (d) Dependence of the fast decay component τ_f on the sample temperature T. The time constant τ_f initially shows a gradual decrease according to $\tau_f \propto T^{-0.08\pm0.03}$ followed by a rapid decrease beyond $T \sim 300$ K that scales as $T^{-1.49\pm0.23}$. The excitation fluence is kept constant at 0.33 mJ/cm^2. (e) Time trace for electron−electron scattering obtained from *ab initio* nonadiabatic molecular dynamics (solid line), which reveals a 37 fs time constant (dashed line exponential fit) for the scattering of carriers. The inset shows the simulated dephasing of carriers (solid line) on a 35 fs time scale (dotted line exponential fit). (f) Zeroth-moment time trace $\langle \lambda^{(0)}(t) \rangle$ computed about the A exciton transition, suggestive of <20 fs intervalley scattering. The solid line is a fit to a biexponential decay convolved with the instrument response function. The excitation fluence is 0.33 mJ/cm^2, and the sample temperature is 77 K.

thermalization rates found for In$_{0.47}$Ga$_{0.53}$As quantum wells with thicknesses spanning the one-dimensional quantum confinement to bulk regimes.[39] Furthermore, recent experimental measurements performed on Al$_x$Ga$_{1-x}$As quantum wells over a larger range of carrier densities than that accessed in ref 37 show unequivocally that carrier−carrier scattering time constants scale as $n^{-1/3}$ even in 2D systems.[40]

The $n^{-1/3}$-dependence observed in the MoS$_2$ sample is suggestive of non-Markovian quantum kinetics. In contrast to Boltzmann kinetics, which treats carrier−carrier scattering events as irreversible processes of negligible durations that are local in both space and

time, non-Markovian quantum kinetics considers the phase-coherent, wave-like nature of the carriers on short time scales, from which finite scattering durations and memory effects emerge, as well as the finite time for the buildup of screening.[41−43] In the presence of carrier phase coherence, the duration of a carrier−carrier scattering event T_{coh} is given by the relation $T_{coh} = h/\Delta E_{coh}$, where ΔE_{coh} is the energy separation between the initial and final states. When T_{coh} becomes comparable to or longer than the interval between successive scattering events, the Fermi Golden Rule-type description of scattering in terms of a single rate, as in semiclassical Boltzmann kinetics, is no longer

applicable. Studies of early time carrier dynamics in the coherent regime must therefore be analyzed within the framework of non-Markovian quantum kinetics. In this work, carrier phase coherence is favored by the coherent excitation of the A and B transitions by broadband 10 fs pulses. Semiclassical evaluation[44] yields an electronic coherence time of 35 fs (Figure 3e inset) that is comparable to the time between successive scattering events. This result lends support to the observation of carrier—carrier scattering in the quantum kinetic regime. The existence of relatively long-lived carrier phase coherence is further complicated by the finite time required for screening to be established, which occurs on the time scale of the inverse plasmon frequency ω_p^{-1}.[45] In fact, it is the retarded quantum-kinetic screening that results in the observed $n^{-1/3}$-dependence of the carrier—carrier scattering times for both 2D and 3D materials;[40,46] by contrast, the initial analysis that gave the $n^{-1/D}$-dependence assumes the instantaneous creation of a short-ranged, strongly screened Coulomb potential by the pump pulse.[36,37] It is important to note that the buildup of screening can be slower in 2D than 3D systems, since ω_p in the case of the former vanishes in the limit of small wave vector.[47] As such, it is conceivable that non-Markovian quantum kinetics manifests itself more strongly in 2D than in 3D systems.

The observed temperature-dependence of τ_f suggests that carrier—phonon scattering also contributes to carrier thermalization. While the effect of temperature on carrier—phonon scattering in MoS_2 remains unexplored by time-resolved studies, information on electron—phonon scattering can nonetheless be inferred from temperature-dependent electron mobility measurements. Indeed, within the relaxation time approximation, the time interval between scattering τ is related to the electron mobility μ by the Drude relation $\mu = e\tau/m^*$, where m^* is the effective electron mass.[48] Our experimental data shows that the gradual decrease in τ_f at low temperatures is followed by a more rapid decrease at higher temperatures (Figure 3d). This behavior is qualitatively similar to the temperature-dependent electron mobility curves exhibited by mono- and bilayer MoS_2 as well as bulk samples.[28,49−51] Analogous to the situation encountered in electron mobility, the plateau in the measured thermalization time constant τ_f at low temperatures can be attributed to charged-impurity scattering counteracting the scattering of carriers by acoustic and optical phonons.[52] At higher temperatures, carrier—phonon scattering dominates and results in the power law $\tau_f \propto T^{-\gamma}$. Despite the experiment being performed on a five-layer MoS_2 sample, it is noteworthy that the measured exponent γ of 1.49 ± 0.23 in the present work is similar to those previously measured ($\gamma = 1.4, 1.7$)[28,49] and predicted ($\gamma = 1.69$)[53] for monolayer MoS_2; in comparison, bulk MoS_2 exhibits a significantly higher γ value of 2.6.[50,51] The observed similarity of the γ values could be coincidental, since measurements and simulations of mobility have focused on that of electrons alone, whereas the time constant τ_f obtained from our pump—probe measurements reflects the dynamics of both electrons and holes.

Further evidence for the participation of carrier—phonon scattering in the sub-20 fs carrier thermalization process comes from examining the zeroth-moment time trace for the bleaching band of the A exciton transition (Figure 3f). The zeroth moment, defined as $\langle \lambda^{(0)}(t) \rangle = \int_{\lambda_i}^{\lambda_f} d\lambda \, \Delta T(\lambda,t)/T(\lambda)$, gives the total population of carriers in the region of k space whose valence and conduction bands are optically coupled by probe wavelengths that span λ_i to λ_f.[54] The $\langle \lambda^{(0)}(t) \rangle$ time trace computed for the A transition exhibits a biphasic decay. The faster component is characterized by a time constant of 15.4 ± 0.2 fs, consistent with that obtained from monitoring the single-wavelength kinetics at 655 nm (14.1 ± 0.3 fs). The decrease of the spectrally integrated stimulated emission signal with time delay is indicative of the rapid scattering of carriers away from the initially populated K valley (the Franck—Condon region). Inspection of the calculated band structures for few-layer MoS_2 suggests that electrons can scatter to the Q valley, located midway between the K and Γ points and where the conduction band minimum resides, whereas holes can scatter to the valence band maximum located at the Γ valley.[38,55] Such intervalley scattering must be phonon-mediated in order to satisfy momentum conservation. Among the various phonons that are present in MoS_2, the longitudinal acoustic (LA) phonon has been identified by first-principles calculations to be the dominant source of intervalley carrier—phonon scattering.[56] In fact, the theoretical total intervalley scattering rate of >0.05 fs^{-1} supports the observed <20 fs thermalization time constant.

Beyond the ultrafast carrier thermalization dynamics, the optical pump—probe data also reveals slower carrier dynamics (Figure 4a). The $\Delta T/T$ time traces obtained at the A and B excitonic transitions decay monoexponentially with time constants τ_s of 0.64 ± 0.01 and 0.54 ± 0.01 ps, respectively. Both excitation fluence- and temperature-dependence measurements show that the time constant τ_s is prolonged by increasing fluence (Figure 4b) and temperature (Figure 4c). The observed behavior is consistent with the hot phonon effect, whereby a large phonon population that results from either higher lattice temperatures or larger photoexcitation fluences, along with a slow phonon relaxation rate (>10 ps; Supporting Information Figure S5), impedes carrier cooling via phonon emission.[57,58] The origin of the τ_s decay constant can therefore be attributed to carrier cooling, in good agreement with the 0.5 ps cooling time predicted by ab initio nonadiabatic molecular dynamics simulations
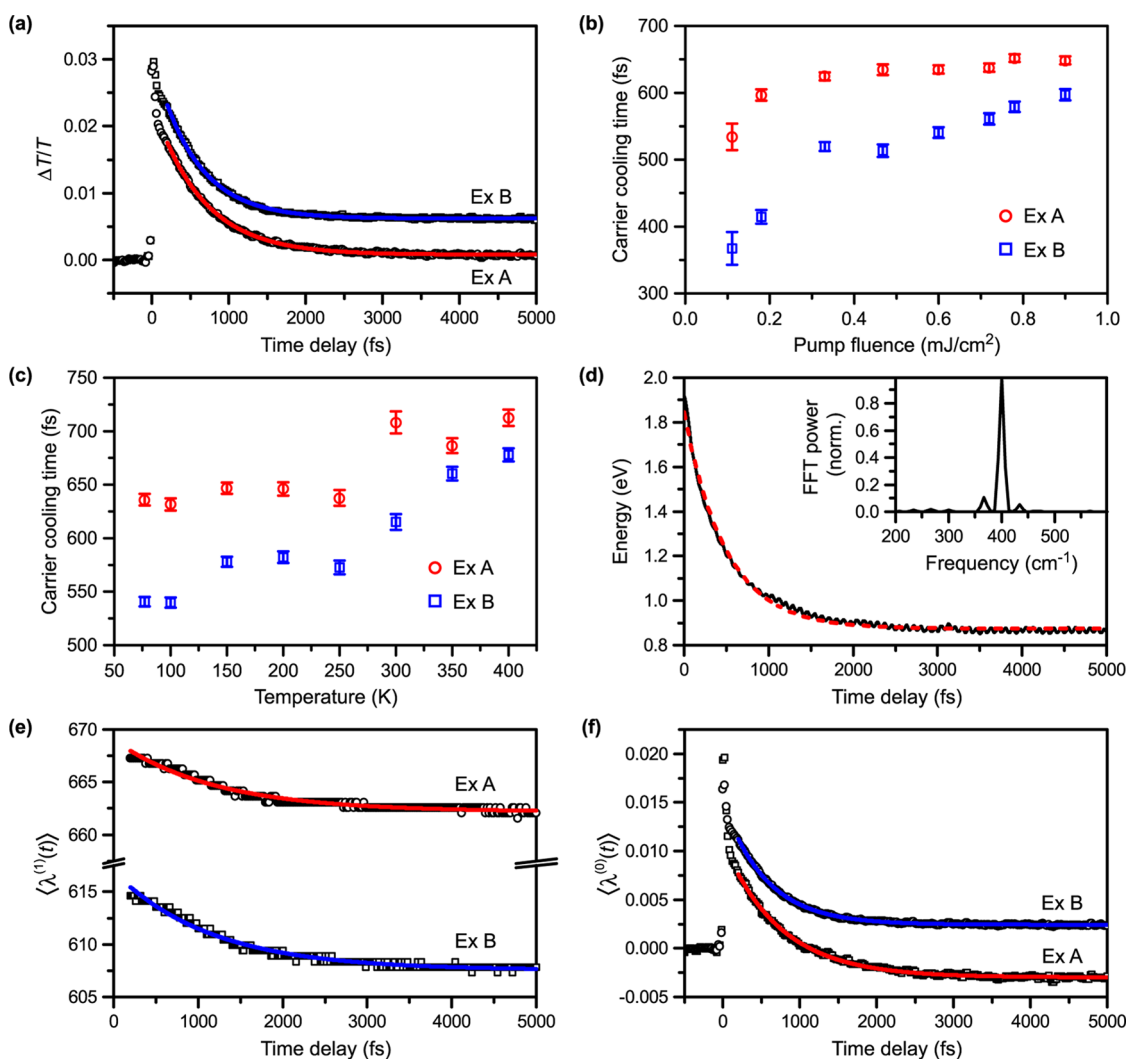
Figure 4. (a) $\Delta T/T$ time traces obtained at the A (○) and B (□) excitonic transitions with 0.33 mJ/cm² excitation fluence and 77 K sample temperature. The solid lines, obtained from fitting the data at time delays >200 fs, reveal slow exponential decay dynamics with a time constant τ_s of ~0.6 ps. (b) Excitation fluence-dependence of τ_s collected at 77 K sample temperature, showing an increase in τ_s with pump fluence. τ_s is determined at both the A (○) and B (□) excitonic transitions. (c) Temperature-dependence of τ_s collected at 0.33 mJ/cm² excitation fluence, showing an increase in τ_s with temperature. τ_s is determined at both the A (○) and B (□) excitonic transitions. (d) Time trace for electron−phonon scattering obtained from *ab initio* nonadiabatic molecular dynamics (solid line), revealing a 0.5 ps decay constant (dashed line exponential fit) for the carrier cooling *via* phonon emission. The inset shows the FFT power spectrum of the calculated time trace, which reveals a dominant component at 400 cm⁻¹ with 33 cm⁻¹ sidebands. (e) First-moment time traces $\langle\lambda^{(1)}(t)\rangle$ computed about the A (○) and B (□) excitonic transitions, showing a blue shift with time delay. The excitation fluence is 0.33 mJ/cm², and the sample temperature is 77 K. The solid lines are fits to exponential shifts of 1.2 ± 0.1 ps. (f) Zeroth-moment time traces $\langle\lambda^{(0)}(t)\rangle$ computed about the A and B exciton transitions, suggestive of ~0.6 ps intervalley scattering.

(Figure 4d). The weak oscillatory feature in the simulated electron cooling time trace with a frequency of 400 cm⁻¹ (Figure 4d inset) is suggestive of the participation of the A_{1g} and/or E^1_{2g} LO phonons[59] in the electron cooling process. We note that the ~0.6 ps time scale for carrier cooling observed in the present work is comparable to the 0.35 ps intervalley scattering time constant that was reported for bulk MoS_2.[27] Under our experimental conditions, however, the excitation fluence-dependence exhibited by the 0.6 ps decay component is incompatible with a previously proposed exciton−exciton scattering process.[25] Contribution from exciton−exciton annihilation, which is expected to accelerate with

increasing excitation pump fluence, can similarly be ruled out based on the observed fluence-dependence.

The above assignment of τ_s to carrier cooling is further supported by the observed blueshift of the spectral first moments of the A and B transitions as a function of time delay. The first moment of an optical transition, defined by the relation $\langle\lambda^{(1)}(t)\rangle = \int d\lambda \ \Delta T(\lambda,t)\lambda/T(\lambda)$,[54] gives the valence-conduction energy gap weighted by the carrier distribution functions. The blueshift of $\langle\lambda^{(1)}\rangle$ for both A and B transitions with increasing time delay (Figure 4e) is indicative of band filling, or the dynamic Burstein−Moss shift, that accompanies intravalley carrier relaxation to the band edge.[60,61] On a

5 ps time scale, the first moments for the A and B excitonic transitions asymptotically approach 662 and 608 nm, respectively; these quasi-equilibrated values are blueshifted relative to the steady-state absorption maxima of the A and B transitions located at 665 and 612 nm, respectively (Figure 1a). The spectral shifts of both transitions occur with a time constant of 1.2 ± 0.1 ps, noticeably different from $\tau_s \sim 0.6$ ps that is associated with the decay of the differential transmission signal. This discrepancy warrants further investigation. Here, we tentatively attribute the existence of two time constants to the separate electron and hole cooling channels, whereby the larger effective mass of the electron than the hole at the K point of MoS_2, as predicted by first-principles calculations ($m_e^*/m_h^* = 1.8$),[62] suggests that the faster process is likely to be associated with electrons.[18] Finally, we note that intervalley scattering also contributes to carrier cooling, as evidenced by the decrease of the zeroth moment of the differential transmission signal with time delay (Figure 4f). The zeroth-moment time traces computed about the A and B excitonic transitions decay with time constants of 0.74 ± 0.01 and 0.55 ± 0.01 ps, respectively, suggestive of intervalley carrier—phonon scattering occurring on these time scales.

CONCLUSION

Femtosecond optical pump—probe spectroscopy with 10 fs pulses has been employed to elucidate the fundamental ultrafast carrier dynamics in five-layer MoS_2. Carrier thermalization is observed to occur on the <20 fs time scale and is found to be mediated via both carrier—carrier and carrier—phonon scattering. The excitation pump fluence-dependence study, which reveals an $n^{-0.37 \pm 0.03}$-scaling of the carrier thermalization time with the carrier density, provides evidence for the existence of non-Markovian quantum kinetic behavior in the carrier—carrier scattering process. Furthermore, the carrier thermalization time exhibits a $T^{-1.49 \pm 0.23}$ temperature-dependence at $T \gtrsim 300$ K, in agreement with previous results obtained from electron mobility studies. The longer, $\sim$0.6 ps decay component is assigned to carrier cooling via phonon emission on account of the observed hot phonon effect. The measured time scales for the above processes are consistent with those obtained from ab initio nonadiabatic molecular dynamics simulations, which yield time constants of 30 fs and 0.5 ps for carrier—carrier and carrier—phonon scattering events, respectively. The ultrafast carrier dynamics of MoS_2 elucidated herein, if applicable to single-layer MoS_2, suggests that valley depolarization via electron—electron and electron—phonon scattering could occur on time scales as short as $\sim$10 fs. More generally, the observed carrier scattering dynamics are expected to shed light on the transport properties of MoS_2 under nonequilibrium conditions.

EXPERIMENTAL METHODS

Optical pump—probe spectroscopy is performed with 10 fs pulses centered at 660 nm with a spectral bandwidth of $\sim$200 nm. These pulses are produced by spectral broadening of the 25 fs output from an amplified Ti:sapphire laser system in a helium-filled hollow-core fiber followed by chirped mirror compression and six bounces off of a broadband dielectric mirror pair with 650 nm center wavelength. A pair of fused silica wedges is used for dispersion fine-tuning. The resultant pulses enter a Mach—Zehnder interferometer, which consists of a motorized translation stage incorporated into the probe arm to generate a computer-controlled time delay between pump and probe pulses. The time resolution of the apparatus is 14 fs (Supporting Information Figure S6), as determined by the width of the second-order intensity cross-correlation between pump and probe pulses. The cross-correlation is performed in a 10-μm-thick BBO crystal located at the position of the sample target. To extract reliable time constants τ_f for the fast decay component, the measured time traces are fit to a convolution of the instrument response function with a biexponential decay function. Typical pulse energies for pump and probe beams are 100 and 20 nJ, respectively; both beams have focal spot diameters ($1/e^2$) of 200 μm. The pump and probe beams are orthogonally polarized to minimize the contribution of coherent artifacts to the measured signal, which can be further suppressed by singular-value decomposition of the two-dimensional probe wavelength-time delay data set (Supporting Information Figure S7).[63] The transmitted probe beam is spectrally dispersed in a 300 mm spectrograph and detected on a 1024-element linear array detector. The detector has a read-out rate of 1 kHz and is synchronized to the 500-Hz optical chopper positioned in the path of the pump beam. Fluence-dependence measurements confirm that the differential transmission signal is linear in the range of pulse energies used in the experiments (Supporting Information Figure S4). The MoS_2 sample is housed in a vacuum cryostat that is evacuated to <10^{-6} mbar to perform the variable temperature measurements. The vacuum environment also minimizes sample degradation by potential atmospheric oxidation over the course of the measurements.

The 5-layer MoS_2 sample is prepared by chemical vapor deposition. The $MoCl_5$ precursor (99.6%, Alfa Aesar) is kept in a bubbler at room temperature and its vapor is delivered by argon gas, which acts only as a carrier gas, through a mass flow controller (MFC) to the CVD quartz tube. The reactive gas, H_2S, is generated in situ by the reaction of 18% aqueous HCl and FeS (99%, Strem) and delivered diluted with argon gas through a second MFC. The H_2S/argon mix is purified by passing through an in-line dryer before entering the CVD reactor. The flow rates for delivering $MoCl_5$ precursor and H_2S are 250 and 200 sccm, respectively. After 25 min, the CVD-grown Mo—S thin films are annealed with H_2 and H_2S mixture gases at 500 °C to remove Cl atoms, followed by an additional annealing process with H_2S gas at 900 °C to convert MoS_3 to MoS_2.

Theoretical Methods. We apply ab initio nonadiabatic molecular dynamics (NAMD) implemented within time-domain density functional theory (TDDFT)[64] to model the electron—electron scattering and electron—phonon relaxation in an 108-atom bilayer MoS_2. The simulations are carried out using the Vienna ab initio simulation package (VASP)[65,66] enhanced with the NAMD capabilities.[67,68] The generalized gradient approximation functional of Perdew, Burke and Ernzerhof[69] and the projector augmented wave approximation for the core electrons[70] are used. The system is periodically replicated in three dimensions. To prevent spurious interactions between the bilayer images, 8 Å of vacuum is added perpendicular to the bilayer. The optimized MoS_2 bilayer is heated to 300 K by

repeated velocity rescaling. A 5 ps microcanonical MD trajectory is generated in the ground state with a 1 fs time step. van der Waals interactions[71] are included to stabilize the bilayer system during geometry optimization and MD simulations. The calculated density of states of the bilayer MoS_2 is shown in Figure S8 of Supporting Information.

To model the photoinduced electron−phonon dynamics in the time-domain, we utilize fewest switches surface hopping (FSSH)[72] implemented within TDDFT with the classical path approximation.[67] FSSH is a NAMD methodology that converts the time-dependent Schrödinger equation into a master-type equation with time-dependent transition rates. With a stochastic algorithm, it accounts for correlation of phonon trajectories with different electronic states, gives trajectory branching, and satisfies detailed balance between transitions upward and downward in energy. The latter property ensures that thermodynamic equilibrium is achieved at long times.[73] The many-electron configurations are expressed using Slater determinants, which are built from the one-electron Kohn−Sham (KS) orbitals. The NA couplings between the many-electron configurations are expressed in terms of the NA couplings between the KS orbitals.[66,67] They are computed numerically using the approximation.[74] A detailed description of the algorithm and discussion of its capabilities and limitations can be found elsewhere.[67,68]

NAMD-TDDFT generates nonequilibrium electron−phonon trajectories, subject to an initial condition. For each configuration in the bilayer MoS_2 system, the initial state was chosen by selecting the adiabatic configuration with the largest optical transition dipole moment from the ground state, within the relevant energy range. To allow both electron−electron and electron−phonon scattering, the simulations include configurations with one and two active electrons and holes. To characterize the carrier phase coherence during the electron−electron scattering we compute the pure-dephasing function, as described in ref 44. The coherence in the electronic subsystem is destroyed due to elastic interactions with the phonon subsystem.

Conflict of Interest: The authors declare no competing financial interest.

Supporting Information Available: Sample characterization by AFM and Raman microscopy, variable-temperature absorption spectroscopy, calculated photoexcited carrier densities and absorbed laser spectrum, excitation pump fluence-dependence measurements, measurement of phonon relaxation time constants, optical pump−probe cross-correlation, suppression of coherent artifact by singular-value decomposition, and calculated density of states for bilayer MoS_2. This material is available free of charge *via* the Internet at http://pubs.acs.org.

REFERENCES AND NOTES

1. Novoselov, K. S.; Geim, A. K.; Morozov, S. V.; Jiang, D.; Zhang, Y.; Dubunos, S. V.; Grigorieva, I. V.; Firsov, A. A. Electric Field Effect in Atomically Thin Carbon Films. *Science* **2004**, *306*, 666–669.
2. Castro Neto, A. H.; Guinea, F.; Peres, N. M. R.; Novoselov, K. S.; Geim, A. K. The Electronic Properties of Graphene. *Rev. Mod. Phys.* **2009**, *81*, 109–162.
3. Butler, S. Z.; Hollen, S. M.; Cao, L.; Cui, Y.; Gupta, J. A.; Gutiérrez, H. R.; Heinz, T. F.; Hong, S. S.; Huang, J.; Ismach, A. F.; *et al.* Progress, Challenges and Opportunities in Two-Dimensional Materials Beyond Graphene. *ACS Nano* **2013**, *7*, 2898–2926.
4. Xu, M.; Liang, T.; Shi, M.; Chen, H. Graphene-like Two-Dimensional Materials. *Chem. Rev.* **2013**, *113*, 3766–3798.
5. Wang, Q. H.; Kalantar-Zadeh, K.; Kis, A.; Coleman, J. N.; Strano, M. S. Electronics and Optoelectronics of Two-Dimensional Transition Metal Dichalcogenides. *Nat. Nanotechnol.* **2012**, *7*, 699–712.
6. Chhowalla, M.; Shin, H. S.; Eda, G.; Li, L.-J.; Loh, K. P.; Zhang, H. The Chemistry of Two-Dimensional Layered Transition Metal Dichalcogenide Nanosheets. *Nat. Chem.* **2013**, *5*, 263–275.
7. Ganatra, R.; Zhang, Q. Few-Layer MoS_2: A Promising Layered Semiconductor. *ACS Nano* **2014**, *8*, 4074–4099.
8. *Gmelin Handbook of Inorganic and Organometallic Chemistry*, 8th ed.; Springer-Verlag: Berlin, 1995; Vol. B7.
9. Splendiani, A.; Sun, L.; Zhang, Y.; Li, T.; Kim, J.; Chim, C.-Y.; Galli, G.; Wang, F. Emerging Photoluminescence in Monolayer MoS2. *Nano Lett.* **2010**, *10*, 1271–1275.
10. Mak, K. F.; Lee, C.; Hone, J.; Shan, J.; Heinz, T. F. Atomically Thin MoS_2: A New Direct-Gap Semiconductor. *Phys. Rev. Lett.* **2010**, *105*, 136805.
11. Radisavljevic, B.; Radenovic, A.; Brivio, J.; Giacometti, V.; Kis, A. Single-Layer MoS_2 Transistors. *Nat. Nanotechnol.* **2011**, *6*, 147–150.
12. Jariwala, D.; Sangwan, V. K.; Lauhon, L. J.; Marks, T. J.; Hersam, M. C. Emerging Device Applications for Semiconducting Two-Dimensional Transition Metal Dichalcogenides. *ACS Nano* **2014**, *8*, 1102–1120.
13. Xiao, D.; Liu, G.-B.; Feng, W.; Xu, X.; Yao, W. Coupled Spin and Valley Physics in Monolayers of MoS_2 and Other Group-VI Dichalcogenides. *Phys. Rev. Lett.* **2012**, *108*, 196802.
14. Cao, T.; Wang, G.; Han, W.; Ye, H.; Zhu, C.; Shi, J.; Niu, Q.; Tan, P.; Wang, E.; Liu, B.; *et al.* Valley-Selective Circular Dichroism of Monolayer Molybdenum Disulphide. *Nat. Commun.* **2012**, *3*, 887.
15. Zeng, H.; Dai, J.; Yao, W.; Xiao, D.; Cui, X. Valley Polarization in MoS_2 Monolayers by Optical Pumping. *Nat. Mater.* **2012**, *7*, 490–493.
16. Mak, K. F.; He, K.; Shan, J.; Heinz, T. F. Control of Valley Polarization in Monolayer MoS_2 by Optical Helicity. *Nat. Mater.* **2012**, *7*, 494–498.
17. Rycerz, A.; Tworzydło, J.; Beenakker, C. W. J. Valley Filter and Valley Valve in Graphene. *Nat. Phys.* **2007**, *3*, 172–175.
18. Shah, J. *Ultrafast Spectroscopy of Semiconductors and Semiconductor Nanostructures*, 2nd ed.; Springer Series in Solid-State Sciences; Springer: Berlin, 1999.
19. Korn, T.; Heydrich, S.; Hirmer, M.; Schmutzler, J.; Schüller, C. Low-Temperature Photocarrier Dynamics in Monolayer MoS_2. *Appl. Phys. Lett.* **2011**, *99*, 102109.
20. Lagarde, D.; Bouet, L.; Marie, X.; Zhu, C. R.; Liu, B. L.; Amand, T.; Tan, P. H.; Urbaszek, B. Carrier and Polarization Dynamics in Monolayer MoS_2. *Phys. Rev. Lett.* **2014**, *112*, 047401.
21. Wang, R.; Ruzicka, B. A.; Kumar, N.; Bellus, M. Z.; Chiu, H.-Y.; Zhao, H. Ultrafast and Spatially Resolved Studies of Charge Carrier in Atomically Thin Molybdenum Disulfide. *Phys. Rev. B* **2012**, *86*, 045406.
22. Shi, H.; Yan, R.; Bertolazzi, S.; Brivio, J.; Gao, B.; Kis, A.; Jena, D.; Xing, H. G.; Huang, L. Exciton Dynamics in Suspended Monolayer and Few-Layer MoS_2 2D Crystals. *ACS Nano* **2013**, *7*, 1072–1080.
23. Wang, Q.; Ge, S.; Li, X.; Qiu, J.; Ji, Y.; Feng, J.; Sun, D. Valley Carrier Dynamics in Monolayer Molybdenum Disulfide from Helicity-Resolved Ultrafast Pump-Probe Spectroscopy. *ACS Nano* **2013**, *7*, 11087–11093.
24. Mai, C.; Barrette, A.; Yu, Y.; Semenov, Y. G.; Kim, K. W.; Cao, L.; Gundogdu, K. Many-Body Effects in Valleytronics: Direct Measurement of Valley Lifetimes in Single-Layer MoS_2. *Nano Lett.* **2014**, *14*, 202–206.
25. Sim, S.; Park, J.; Song, J.-G.; In, C.; Lee, Y.-S.; Kim, H.; Choi, H. Exciton Dynamics in Atomically Thin MoS_2: Interexcitonic

Interaction and Broadening Kinetics. *Phys. Rev. B* **2013**, *88*, 075434.

26. Tanaka, A.; Watkins, N. J.; Gao, Y. Hot-Electron Relaxation in the Layered Semiconductor 2H-MoS₂ Studied by Time-Resolved Two-Photon Photoemission Spectroscopy. *Phys. Rev. B* **2003**, *67*, 113315.

27. Kumar, N.; He, J.; He, D.; Wang, Y.; Zhao, H. Charge Carrier Dynamics in Bulk MoS₂ Crystal Studied by Transient Absorption Microscopy. *J. Appl. Phys.* **2013**, *113*, 133702.

28. Radisavljevic, B.; Kis, A. Mobility Engineering and a Metal-Insulator Transition in Monolayer MoS₂. *Nat. Mater.* **2013**, *12*, 815–820.

29. Oudar, J. L.; Hulin, D.; Migus, A.; Antonetti, A.; Alexandre, F. Subpicosecond Spectral Hole Burning Due to Nonthermalized Photoexcited Carriers in GaAs. *Phys. Rev. Lett.* **1985**, *55*, 2074–2077.

30. Knox, W. H.; Hirlimann, C.; Miller, D. A. B.; Shah, J.; Chemla, D. S.; Shank, C. V. Femtosecond Excitation of Nonthermal Carrier Populations in GaAs Quantum Wells. *Phys. Rev. Lett.* **1986**, *56*, 1191–1193.

31. Völker, S. Hole-Burning Spectroscopy. *Annu. Rev. Phys. Chem.* **1989**, *40*, 499–530.

32. Brito Cruz, C. H.; Gordon, J. P.; Becker, P. C.; Fork, R. L.; Shank, C. V. Dynamics of Spectral Hole Burning. *IEEE J. Quantum Electron.* **1988**, *24*, 261–266.

33. Wang, K.; Wang, J.; Fan, J.; Lotya, M.; O'Neill, A.; Fox, D.; Feng, Y.; Zhang, X.; Jiang, B.; Zhao, Q.; *et al.* Ultrafast Saturable Absorption of Two-Dimensional MoS₂ Nanosheets. *ACS Nano* **2013**, *7*, 9260–9267.

34. Brida, D.; Tomadin, A.; Manzoni, C.; Kim, Y. J.; Lombardo, A.; Milana, S.; Nair, R. R.; Novoselov, K. S.; Ferrari, A. C.; Cerullo; *et al.* Ultrafast Collinear Scattering and Carrier Multiplication in Graphene. *Nat. Commun.* **2013**, *4*, 1987.

35. Breusing, M.; Ropers, C.; Elsaesser, T. Ultrafast Carrier Dynamics in Graphite. *Phys. Rev. Lett.* **2009**, *102*, 086809.

36. Becker, P. C.; Fragnito, H. L.; Brito Cruz, C. H.; Fork, R. L.; Cunningham, J. E.; Henry, J. E.; Shank, C. V. Femtosecond Photon Echoes from Band-to-Band Transitions in GaAs. *Phys. Rev. Lett.* **1988**, *61*, 1647–1649.

37. Bigot, J.-Y.; Portella, M. T.; Schoenlein, R. W.; Cunningham, J. E.; Shank, C. V. Two-Dimensional Carrier-Carrier Screening in a Quantum Well. *Phys. Rev. Lett.* **1991**, *67*, 636–639.

38. Molina-Sánchez, A.; Sangalli, D.; Hummer, K.; Marini, A.; Wirtz, L. Effect of Spin-Orbit Interaction on the Optical Spectra of Single-Layer, Double-Layer, and Bulk MoS2. *Phys. Rev. B* **2013**, *88*, 045412.

39. Bolton, S.; Sucha, G.; Chemla, D.; Sivco, D. L.; Cho, A. Y. Effects of Confinement on Carrier Dynamics in In₀.₄₇Ga₀.₅₃As Heterostructures. *Phys. Rev. B* **1998**, *58*, 16326–16332.

40. Mieck, B.; Haug, H.; Hügel, W. A.; Heinrich, M. F.; Wegener, M. Quantum-Kinetic Dephasing in Resonantly Excited Semiconductor Quantum Wells. *Phys. Rev. B* **2000**, *62*, 2686–2695.

41. Chemla, D. S.; Shah, J. Many-Body and Correlation Effects in Semiconductors. *Nature* **2001**, *411*, 549–557.

42. Axt, V. M.; Kuhn, T. Femtosecond Spectroscopy in Semiconductors: A Key to Coherences, Correlations and Quantum Kinetics. *Rep. Prog. Phys.* **2004**, *67*, 433–512.

43. Haug, H.; Jauho, A.-P. *Quantum Kinetics in Transport and Optics of Semiconductors*, 2nd ed.; Springer Series in Solid-State Sciences; Springer: Berlin, 2008.

44. Madrid, A. B.; Kim, H.-D.; Habenicht, B. F.; Prezhdo, O. V. Phonon-Induced Dephasing of Excitons in Silicon Quantum Dots: Multiple Exciton Generation, Fission and Luminescence. *ACS Nano* **2009**, *3*, 2487–2494.

45. El Sayed, K.; Schuster, S.; Haug, H.; Herzel, F.; Henneberger, K. Subpicosecond Plasmon Response: Buildup of Screening. *Phys. Rev. B* **1994**, *49*, 7337–7344.

46. Hügel, W. A.; Heinrich, M. F.; Wegener, M.; Vu, Q. T.; Bányai, L.; Haug, H. Photon Echoes from Semiconductor Band-to-Band Continuum Transitions in the Regime of Coulomb Quantum Kinetics. *Phys. Rev. Lett.* **1999**, *83*, 3313–3316.

47. Stern, F. Polarizability of a Two-Dimensional Electron Gas. *Phys. Rev. Lett.* **1967**, *18*, 546–548.

48. Klingshirn, C. *Semiconductor Optics*, 2nd ed.; Springer: Berlin, 2005; pp 571−644.

49. Baugher, B. W. H.; Churchill, H. O. H.; Yang, Y.; Jarillo-Herrero, P. Intrinsic Electronic Transport Properties of High-Quality Monolayer and Bilayer MoS₂. *Nano Lett.* **2013**, *13*, 4212–4216.

50. Fivaz, R.; Mooser, E. Mobility of Charge Carriers in Semiconducting Layer Structures. *Phys. Rev.* **1967**, *163*, 743–755.

51. Kim, S.; Konar, A.; Hwang, W.-S.; Lee, J. H.; Lee, J.; Yang, J.; Jung, C.; Kim, H.; Yoo, J.-B.; Choi, J.-Y.; *et al.* High-Mobility and Low-Power Thin-Film Transistors Based on Multilayer MoS₂ Crystals. *Nat. Commun.* **2012**, *3*, 1011.

52. Ma, N.; Jena, D. Charge Scattering and Mobility in Atomically Thin Semiconductors. *Phys. Rev. X* **2014**, *4*, 011043.

53. Kaasbjerg, K.; Thygesen, K. S.; Jacobsen, K. W. Phonon-Limited Mobility in n-Type Single-Layer MoS₂ from First Principles. *Phys. Rev. B* **2012**, *85*, 115317.

54. Pollard, W. T.; Lee, S.-Y.; Mathies, R. A. Wave Packet Theory of Dynamic Absorption Spectra in Femtosecond Pump-Probe Experiments. *J. Chem. Phys.* **1990**, *92*, 4012–4029.

55. Kuc, A.; Zibouche, N.; Heine, T. Influence of Quantum Confinement on the Electronic Structure of the Transition Metal Sulfide TS2. *Phys. Rev. B* **2011**, *83*, 245213.

56. Li, X.; Mullen, J. T.; Jin, Z.; Borysenko, K. M.; Nardelli, M. B.; Kim, K. W. Intrinsic Electrical Transport Properties of Monolayer Silicene and MoS₂ from First Principles. *Phys. Rev. B* **2013**, *87*, 115418.

57. Shah, J.; Pinczuk, A.; Gossard, A. C.; Wiegmann, W. Energy-Loss Rates for Hot Electrons and Holes in GaAs Quantum Wells. *Phys. Rev. Lett.* **1985**, *54*, 2045–2048.

58. Breusing, M.; Kuehn, S.; Winzer, T.; Malić, E.; Milde, F.; Severin, N.; Rabe, J. P.; Ropers, C.; Knorr, A.; Elsaesser, T. Ultrafast Nonequilibrium Carrier Dynamics in a Single Graphene Layer. *Phys. Rev. B* **2011**, *83*, 153410.

59. Lee, C.; Yan, H.; Brus, L. E.; Heinz, T. F.; Hone, J.; Ryu, S. Anomalous Lattice Vibrations of Single- and Few-Layer MoS₂. *ACS Nano* **2010**, *4*, 2695–2700.

60. Shank, C. V.; Fork, R. L.; Leheny, R. F.; Shah, J. Dynamics of Photoexcited GaAs Band-Edge Absorption with Subpicosecond Resolution. *Phys. Rev. Lett.* **1979**, *42*, 112–115.

61. Erskine, D. J.; Taylor, A. J.; Tang, C. L. Dynamic Burstein-Moss Shift in GaAs and GaAs/AlGaAs Multiple Quantum Well Structures. *Appl. Phys. Lett.* **1984**, *45*, 1209–1211.

62. Qiu, D. Y.; da Jornada, F. H.; Louie, S. G. Optical Spectrum of MoS₂: Many-Body Effects and Diversity of Exciton States. *Phys. Rev. Lett.* **2013**, *111*, 216805.

63. Dobryakov, A. L.; Kovalenko, S. A.; Ernsting, N. P. Electronic and Vibrational Coherence Effects in Broadband Transient Absorption Spectroscopy with Chirped Supercontinuum Probing. *J. Chem. Phys.* **2003**, *119*, 988–1002.

64. Craig, C. F.; Duncan, W. R.; Prezhdo, O. V. Trajectory Surface Hopping in the Time-Dependent Kohn-Sham Approach for Electron-Nuclear Dynamics. *Phys. Rev. Lett.* **2005**, *95*, 163001.

65. Kresse, G.; Furthmüller, J. Efficient Iterative Schemes for *ab Initio* Total-Energy Calculations Using a Plane-Wave Basis Set. *Phys. Rev. B* **1996**, *54*, 11169–11186.

66. Kresse, G.; Hafner, J. *Ab Initio* Molecular Dynamics for Liquid Metals. *Phys. Rev. B* **1993**, *47*, 558–561.

67. Akimov, A. V.; Prezhdo, O. V. The PYXAID Program for Non-Adiabatic Molecular Dynamics in Condensed Matter Systems. *J. Chem. Theory Comput.* **2013**, *9*, 4959–4972.

68. Akimov, A. V.; Prezhdo, O. V. Advanced Capabilities of the PYXAID Program: Integration Schemes, Decoherence Effects, Multiexcitonic States, and Field-Matter Interaction. *J. Chem. Theory Comput.* **2014**, *10*, 789–804.

69. Perdew, J. P.; Burke, K.; Ernzerhof, M. Generalized Gradient Approximation Made Simple. *Phys. Rev. Lett.* **1996**, *77*, 3865–3868.

70. Blöchl, P. E. Projector Augmented-Wave Method. *Phys. Rev. B* **1994**, *50*, 17953–17979.

71. Grimme, S. Semiempirical GGA-Type Density Functional Constructed with a Long-Range Dispersion Correction. *J. Comput. Chem.* **2006**, *27*, 1787–1799.

72. Tully, J. C. Molecular Dynamics with Electronic Transitions. *J. Chem. Phys.* **1990**, *93*, 1061–1071.

73. Parandekar, P. V.; Tully, J. C. Mixed Quantum-Classical Equilibrium. *J. Chem. Phys.* **2005**, *122*, 094102.

74. Long, R.; English, N. J.; Prezhdo, O. V. Photo-Induced Charge Separation Across the Graphene-TiO$_2$ Interface is faster than Energy Losses: A Time-Domain *ab Initio* Analysis. *J. Am. Chem. Soc.* **2012**, *134*, 14238–14248.